Analytical Design of Contributions of Grid-Forming & Grid-Following Inverters to Frequency Stability

Eugenie A. S. Ducoin, *Student Member, IEEE,* Yunjie Gu, *Senior Member, IEEE,* Balarko Chaudhuri, *Senior Member, IEEE,* Timothy C. Green, *Fellow, IEEE*

***Abstract*—Most of the new renewable generation in power systems is connected through Grid-Following inverters (GFL). The accompanying decline of fossil-fuelled synchronous generation reduces the grid inertia. As these two trends progress, instabilities become more likely. To allow more renewables onto the grid, the use of combinations of GFL and Grid-Forming inverters (GFM) has been proposed, however, it is unclear how to parametrise these inverters for system objectives. This paper tackles the issue of parametrizing each GFM and GFL to ensure frequency trajectories at all buses, expressed in terms of frequency deviation, Rate of Change of Frequency and settling time, are stable, recognising that local frequencies can deviate substantially from the Center of Inertia (COI). The procedure to achieve this comprises simple closed-form equations, and yields the required values of droop slopes, GFM filter bandwidth and GFL Phase-Locked Loop bandwidth. These equations are derived from an analytical formulation of swing equations for GFM and GFL which are combined to describe the behaviour of not only the COI but also each bus. The detailed EMT simulations of a modified IEEE 14-bus network demonstrate that the simplifying assumptions made in the analysis are justified by the close correspondence between simulation and analytical projections.**

***Index Terms*—center of inertia, frequency stability, grid-following inverter, grid-forming inverter, RoCoF, swing equation**

I. Introduction

TO achieve decarbonisation of the electrical sector, the volume of renewable sources will need to continue to increase [1]. Most of these sources, such as wind turbines, solar panels and batteries, are connected to the network through inverters whose dynamics are different from those of the traditional Synchronous Generators (SG). In contrast to SG, which present as voltage sources with inherent inertia, the behaviour of Inverter Based Resources (IBR) depends largely on their software-defined controllers [2]. Many variations of controllers have been proposed, and most can be classified into two main types: Grid Following (GFL) and Grid Forming (GFM) inverters. The former acts as a current source that follows the grid frequency and voltage, and the latter presents as a voltage source that forms the grid frequency and voltage [2]. Since 2020, the grid code in Great Britain (GB) has allowed implementation of GFM capabilities, mainly in the form of power-frequency droop control [3]. However, GFL is still the main type of inverter in the GB grid despite drawbacks such as Phase Locked Loop (PLL) instabilities [4] and absence of inertia provision [5].

The decline in inertia as GFL IBR displace SG is a major concern for the GB System Operator (SO), National Grid ESO, as evident in its System Operability Framework [6]. The frequency of a system with little inertia varies more rapidly after a power imbalance, giving less time for the SO to call-up appropriate recovery measures. Further, Rate of Change of Frequency (RoCoF) and frequency deviation are metrics used by many apparatuses to assess the safety of a connection. One common form of Loss-of-Mains frequency protection scheme measures the RoCoF to determine if a part of the network is islanded [7], and disconnection of generation occurs if thresholds are exceeded. If the system inertia is too low and a large power imbalance occurs, high RoCoF might be measured and mistaken for an islanding. RoCoF relays could be triggered, worsening the initial power imbalance and potentially leading to load shedding [4].

GFM inverters can provide inertia [5], and many control schemes have been proposed. Generally, the inertia is a function of control parameters and can be configured to help to regulate the trajectory of the system frequency. The base scheme applies a Low-Pass Filter (LPF) to the measured output power before it is used in a power-frequency droop function. The LPF slows the response of the GFM frequency to a power imbalance thereby providing virtual inertia. The combination of droop slope and filter bandwidth defines the inertia of the GFM [8]. Alternatively, Virtual Synchronous Machines (VSM) implement the SG equations within the inverter controller, mimicking SG inertia.

Tools and analyses to solve frequency stability issues have been proposed for the planning and operation of the grid with high penetration level of IBR. Traditionally, the swing equation is used for frequency stability. It relates the RoCoF and frequency deviation of SG to the power imbalance between mechanical and electrical powers [9]. It is simple, ubiquitous and well-understood by the community. To capture dynamics specific to IBR, electromechanical models have been developed that accurately represent the impact of inverters on an electrical system. [10] and [11] develop a positive sequence model for a generic IBR controller. [12] evaluates the frequency support provided by different types of IBR through simulations. [13] presents detailed and accurate GFM and GFL models for dynamic analysis. While the models are useful to study IBR dynamics, they are complex and take a long time to simulate [13].

The authors are with the department of Electrical and Electronic Engineering, Imperial College London, London, UK

This work was supported by a PhD studentship from the Engineering and Physical Sciences Research Council (EPSRC) [EP/N509486/1]. For the purpose of open access, the authors have applied a Creative Commons Attribution (CC BY) licence to any Author Accepted Manuscript version arising.

From an operation perspective, an SO needs analytical procedures that allow them to design the trajectory of the system frequency quickly. Frequency-Trajectory Planning attempts to maintain the frequency deviation and RoCoF within defined bounds by measuring said parameters and adjusting the inertia in real-time [14]. However, a PLL is used to measure the frequency, and this can cause instabilities and delays [4]. [15] and [16] also offer self-adaptive inertia schemes for VSG to obtain optimal local frequency trajectory. Those schemes which adapt their parameters in response to the measured frequency focus on the local need for inertia and do not consider the wider system. Local frequency and RoCoF can vary greatly around the Centre of Inertia (COI) [17]. COI is the weighted average of the frequency at all buses, weighted by inertia [18]. An SO facing a high RoCoF in an area with few resources for offering improvement might be obliged to choose to boost the inertia of an adjacent area.

Between computationally heavy models and online IBR tuners, methods have been proposed to shape the frequency trajectory in the short-term based on the steady state operating point of the grid at the time of analysis. [19] models the network with linearized swing equations and proposes an optimization problem for the placement of inertia to be used for planning or scheduling. It is an iterative solution that relies on the knowledge of the eigenvalues of the system which can be computationally costly to find. Besides, [19] does not consider inverter models or whether they can provide virtual inertia. [20] uses swing equations to optimize the COI nadir and steady state frequency based on an economic cost. However, it does not differentiate between GFL and GFM, and local bus frequencies and local RoCoF are not studied. [21] formulates an optimization problem for the placement of inertia that also considers the parametrization of GFL and GFM inverters, but its complexity does not allow for analytical insights. [22] proposes a GFM control scheme to shape the COI frequency trajectory, in terms of nadir and RoCoF, through the tuning of controller parameters, but it does not consider contributions from GFL.

[8] and [23] propose swing equation models for GFM and GFL respectively. This paper uses these models to offer analytical insights into the contributions of GFM and GFL to frequency stability, and it proposes a procedure with closed-form equations for an SO to design the local RoCoF at all buses, the steady state frequency and the settling time based on IBR parametrization at each settlement period. The contributions of this paper are as follows.

1) The format of swing equations for SG, GFM and GFL proposed respectively in [9], [8] and [23] is unified to allow the calculation of the trajectory of local bus frequencies in a composite grid. They are further combined in a swing equation and transfer function for the global COI frequency.

2) Closed-form formulae are proposed to characterize the trajectories of global COI frequency and of local bus frequencies. The formulae for the local RoCoF at a GFL bus and settling time are novel.

3) Using the analysis from 1) and 2), a procedure is proposed for an SO to configure the system to obtain acceptable trajectories of local frequencies in terms of frequency deviation, RoCoF and settling time.

The remainder of the paper is organised as follows. Section II presents the modelling of IBR and COI as swing equations and the analysis of the model to characterise the local and global frequency deviation, RoCoF and settling time. The analyses are verified in Section III on a modified IEEE 14-bus network. Section IV proposes a procedure based on the analysis of Section II to design the trajectory of the system frequency. The procedure is validated on the modified IEEE 14-bus network. Finally, Section V concludes the paper.

II. Analysis of the transient power-frequency response

The power-frequency transient response of GFM and GFL with droop control is studied in this section.

A. Assumptions (for analysis only)

Typical controllers are shown in Fig. 1 although the analysis would apply also to inverters with different controllers provided the red parts (droop functions, and LPF or PLL) are present. Classic VSM schemes are also equivalent to the GFM in Fig. 1a [8], and an example of a GFL with an additional droop function based on the measured RoCoF is presented in Appendix C. It is assumed that the inner-loops of controllers, that is, current controllers, and voltage controllers for GFM or power controllers for GFL, are perfect. The PLL tracking delay is not ignored since in an IBR-based network, the inertia is expected to be low, the frequency variations could be fast, and the PLL tracking delay of a large RoCoF might be significant. It is assumed that any requirement for additional power associated with inertia can be met by appropriate reserves. For the inertial response immediately after an event, a sufficient energy buffer should be provided, and also power can be extracted from, for example, the mechanical inertia of wind turbines [24] or from storage resources such as DC capacitors [25], [26] or batteries [27]. These energy buffers allow time to access the reserves for primary response which, for a renewable resource, generally means de-loading it below its maximum power point (at that point in time) to allow headroom for increasing power [28]. A resource that does not have sufficient power reserves would not be expected to provide frequency response services. A renewable resource that is not able to quickly deliver additional power through these methods would not offer frequency response services to the SO and instead operate as a simple GFL without droop. The assumption that additional power is readily available implies that the variability of power that is intrinsic to renewable resources and non-linearities such as limitation of primary energy are ignored. Extensive research has been done on forecasting renewable resources [29], [30], and it is assumed that short-term forecast models (around 30 minutes) are reliable enough to use the analysis in this paper for the regulation market timescale without hitting such limitations. An SO may choose to over-contract for inertia and damping to manage the risk of some resources failing to deliver the service when called upon.

The network is assumed lossless, and the lines are considered as a constant reactance with no dependency on the

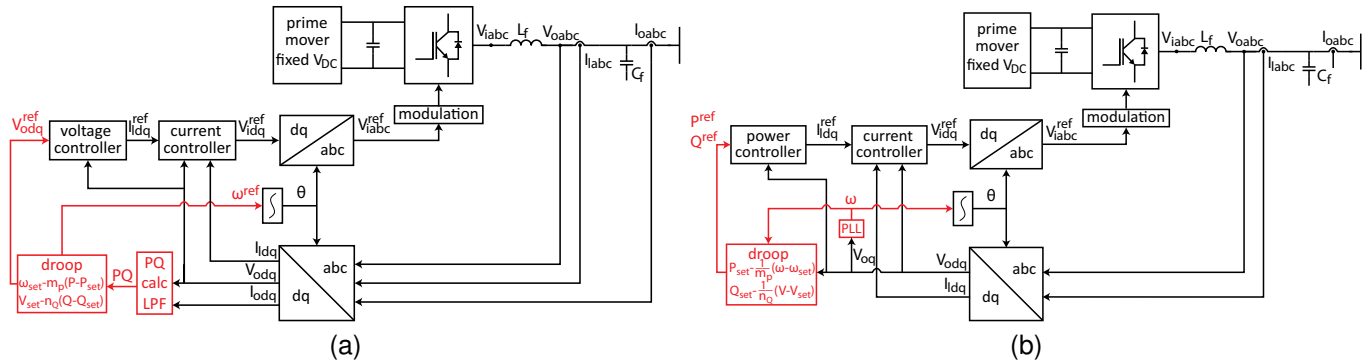


Fig. 1. Controller diagram for (a) GFM and (b) GFL.

frequency. With the focus on frequency stability, voltage magnitudes are assumed constant, and the grid is therefore voltage-strong. Since GFM can strengthen the grid voltage [31], it is assumed that there are enough GFM or SG to ensure voltage stability. The frequency strength of the grid is the focus in this paper, and it is assumed that angle and small-signal stability have been ensured first.

In Sections II-C, II-D and II-F, when deriving the COI transfer function, steady-state frequency deviation and settling time, frequency oscillations around the COI are assumed negligible. This assumption is valid only when studying the long-term dynamics of COI [32], so it is not used when deriving the swing equations for local frequencies (Section II-B) and RoCoF at each bus (Section II-E).

Most of these assumptions are not made in the simulations of Sections III and IV, but one is retained: that there is no limit on power provided by IBR (their DC-link is a voltage source), which is mitigated by assuming that the available power is known through reliable forecasts and appropriate hardware.

B. Swing equations

Swing equations have been used to study the frequency trajectory of SG-based networks for decades [9], and they are widely used and understood. This section simplifies IBR's power-frequency dynamics, and the results are analogous to the SG swing equation. Although swing equations do not incorporate the fast controller dynamics of IBR, their simplicity reveals insights and rules of thumb that can be used as a starting point to locate stable conditions of systems that undergo frequent changes of operating point.

1) Synchronous Generator: A transfer function for the frequency-power relationship of SG is obtained from Fig. 2 [33] as (1).

$$\left(2H_i^{SG}s + D_i^{SG} + K_iG_i(s)\right)\Delta\omega_i = -\Delta P_i \tag{1}$$

with $G_i(s) = \frac{1}{1+sT_{1_i}}\frac{1}{1+sT_{2_i}}\frac{1+sF_iT_{3_i}}{1+sT_{3_i}}$ and where the subscript i denotes a quantity at bus i, $\Delta\omega_i = \omega_i - \omega_{set}$, ω_i is the frequency, ω_{set} is the frequency setpoint, ΔP_i is the difference between mechanical and electrical power, H_i^{SG} is the SG inertia, D_i^{SG} is the damping contribution from SGs and frequency-dependent loads, K_i is the governor constant, T_{1_i}, T_{2_i} and T_{3_i} are respectively the servomotor, valve bowl and re-heater time constants, and F_i is the fraction of thermal energy converted to mechanical work by the high-pressure turbine [33]. The damping, D_i^{SG}, in the SG swing equation is small, and it is the governor droop and dynamics, $K_iG_i(s)$, that mostly impact the frequency deviation. Hence, this extra term must be included to study the frequency trajectory.

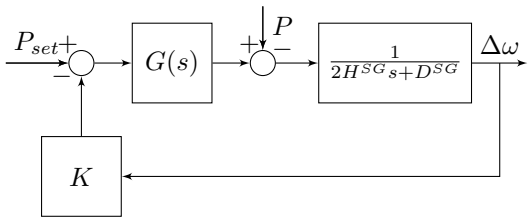


Fig. 2. Block diagram of a reheat turbine speed control [33]

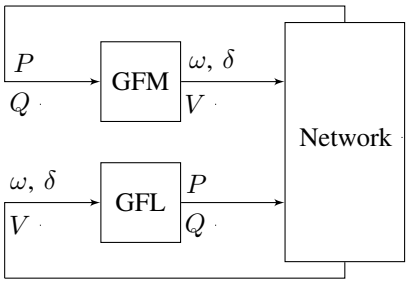


Fig. 3. Network diagram

2) Grid-Forming inverter: The GFM droop in (2) and its LPF for the measured output power in (3) are combined to derive a swing equation (4) for GFM inverters [8]. It is assumed that the inner control loops of inverters track their references perfectly, and $\omega_i = \omega_i^{ref}$.

$$\Delta\omega_i^{ref} = \Delta\omega_i = -m_{P_i}\Delta P_i^f \tag{2}$$

$$\Delta P_i^f = \frac{\omega_{Pf_i}}{s+\omega_{Pf_i}}\Delta P_i \tag{3}$$

$$\frac{1}{m_{P_i}\omega_{Pf_i}}s\Delta\omega_i + \frac{1}{m_{P_i}}\Delta\omega_i = -\Delta P_i \tag{4}$$

where $\Delta\omega_i^{ref} = \omega_i^{ref} - \omega_{set}$, ω_i^{ref} is the reference for the frequency, m_{P_i} is the droop slope of the inverter, $\Delta P_i^f = P_i^f - P_{set_i}$, P_i^f is the filtered output power, P_{set_i} is the power

setpoint, ω_{Pf_i} is the bandwidth of the GFM LPF, $\Delta P_i = P_i - P_{set_i}$, and P_i is the power generated.

The power delivered by the inverter is $P_i = P_{L_i} + \sum_j^n P_{ij}$; it is the sum of the load, P_{L_i}, and of the power flows between bus i and bus j, P_{ij}, with n the total number of buses. Note that the power flows are a function of voltage angles δ with $P_{ij} = \frac{V_i V_j}{X_{ij}} \sin(\delta_i - \delta_j)$, where V is the voltage magnitude and X is the line reactance. Since $\omega_i = s\delta_i$, (4) is a second order differential equation. As shown in Fig. 3, the power is considered as an input to the GFM and the frequency as an output to the GFM and state for the network.

We use $H_i^{GFM} = \frac{1}{2m_{P_i}\omega_{Pf_i}}$ as the GFM inertia and $D_i^{GFM} = \frac{1}{m_{P_i}}$ as the GFM damping and rewrite (4) as (5). Compared to the SG swing equation, the GFM damping, D_i^{GFM}, is similar to the SG governor droop K_i^{SG}, but its impact is not delayed by $G_i(s)$. Hence, GFM are expected to adjust their frequency output faster than SG. The GFM inertia is not provided by an inertia emulation function but by the combination of the LPF and droop control blocks. The action of the LPF means that a step-increase in output power is filtered to become a gradual increase with a rate set by the LPF bandwidth, ω_{Pf_i} which in turn gives a gradual change in frequency (proportional to the droop slope, m_{P_i}). This behavior is analogous to inertia and gives a RoCoF defined by the low-pass filtered increase in power. Hence, both ω_{Pf_i} and m_{P_i} define the GFM inertia.

$$\left(2H_i^{GFM}s + D_i^{GFM}\right)\Delta\omega_i = -\Delta P_i \tag{5}$$

3) Grid-Following inverter: A swing equation for GFL inverters is derived from its PLL characteristics (6) and droop (7) as set out in [23].

$$\omega_i^c = \frac{2\zeta_i\omega_{pll_i}s + \omega_{pll_i}^2}{s^2 + 2\zeta_i\omega_{pll_i}s + \omega_{pll_i}^2}\omega_i \tag{6}$$

$$\Delta P_i = -\frac{1}{m_{P_i}}\Delta\omega_i^c \tag{7}$$

where ω_i^c is the frequency of the GFL PLL, and ζ_i and ω_{pll_i} are, respectively, the damping and bandwidth of the GFL PLL.

Equations (6) and (7) are combined into (8).

$$\Delta P_i = -\frac{\frac{1}{m_{P_i}}\frac{2\zeta_i}{\omega_{pll_i}}s + \frac{1}{m_{P_i}}}{\frac{1}{\omega_{pll_i}^2}s^2 + \frac{2\zeta_i}{\omega_{pll_i}}s + 1}\Delta\omega_i \tag{8}$$

We use $H_i^{GFL} = \frac{1}{m_{P_i}}\frac{\zeta_i}{\omega_{pll_i}}$ as the GFL inertia term and $D_i^{GFL} = \frac{1}{m_{P_i}}$ as the GFL damping and rewrite (8) as (9). (9) looks like the SG swing equation delayed by a second order filter due to the PLL. For GFL, the frequency appears as an input and the power as output. When considering the whole network, the frequency and angles are states calculated through the network admittance matrix, as shown in Fig. 3. The GFL inertia term is formed by the PLL and droop control. A change of frequency at the bus is measured by the PLL with a bandwidth of ω_{pll_i}, then this measured frequency is used by the droop function with a slope of m_{P_i} to define the power reference. Hence, ω_{pll_i} and m_{P_i} define the GFL inertia. However, inertia is usually expected to impact the RoCoF directly, but the impact of H_i^{GFL} on the RoCoF, $s\Delta\omega_i$, is delayed by the PLL that appears as a LPF in (9). So GFL are not expected to provide traditional inertia.

$$\Delta P_i = -\frac{2H_i^{GFL}s + D_i^{GFL}}{\frac{1}{\omega_{pll_i}^2}s^2 + \frac{2\zeta_i}{\omega_{pll_i}}s + 1}\Delta\omega_i \tag{9}$$

4) Centre of Inertia: The frequency at the COI is defined by (10) [18].

$$\Delta\omega_{COI} = \frac{1}{H_T}\sum_i^n H_i\Delta\omega_i \tag{10}$$

with $\Delta\omega_{COI} = \omega_{COI} - \omega_{set}$, where ω_{COI} is the COI frequency and $H_T = \sum_i^n H_i$ is the total inertia. Each bus frequency can deviate around the COI as $\omega_i = \omega_{COI} + \omega_{osc_i}$ where ω_{osc_i} is the oscillation around the COI of the local frequency at bus i. In an IBR-dominated grid, each bus frequency may deviate substantially from the COI, and each IBR swing equation should be considered. However, SOs do place value on the COI frequency, often referred as system frequency, and a COI swing equation is presented in this section. Limitations of the COI will be discussed in Section III.

To derive a swing equation for the COI of an IBR network, (9) is re-written as (11), and (5) and (11) are summed over the total number of GFM, n_{GFM}, and GFL, n_{GFL}.

$$\begin{aligned}&\left(2H_i^{GFL}s + D_i^{GFL}\right)\Delta\omega_i \\ &\qquad = -\left(\frac{1}{\omega_{pll_i}^2}s^2 + \frac{2\zeta_i}{\omega_{pll_i}}s + 1\right)\Delta P_i\end{aligned} \tag{11}$$

Consider first the summation on the left-hand side of both equations: the inertia and damping of both GFM and GFL are expressed as H_i and D_i, and the definition of COI (10) is used in (12).

$$\begin{aligned}&\sum_i^{n_{GFM}}\left(2H_i^{GFM}s + D_i^{GFM}\right)\Delta\omega_i \\ &\qquad + \sum_i^{n_{GFL}}\left(2H_i^{GFL}s + D_i^{GFL}\right)\Delta\omega_i \\ &\qquad = \sum_i^n 2H_i s\Delta\omega_i + \sum_i^n D_i\Delta\omega_i \\ &= 2H_T s\left(\frac{1}{H_T}\sum_i^n H_i\Delta\omega_i\right) + \sum_i^n D_i(\omega_i - \omega_{set}) \\ &= 2H_T s\Delta\omega_{COI} + \sum_i^n D_i(\omega_{COI} + \omega_{osc_i} - \omega_{set}) \\ &= (2H_T s + D_T)\Delta\omega_{COI} + \sum_i^n D_i\omega_{osc_i}\end{aligned} \tag{12}$$

where $D_T = \sum_i^n D_i$ is the total damping.

The right-hand side of (5) and (11) are also summed in (13) with ΔP_i expressed as $P_{L_i} + \sum_j^n P_{ij} - P_{set_i}$.

$$-\sum_i^{n_{GFM}}\Delta P_i - \sum_i^{n_{GFL}}\left(\frac{1}{\omega_{pll_i}^2}s^2 + \frac{2\zeta_i}{\omega_{pll_i}}s + 1\right)\Delta P_i$$

$$= - \sum_{i}^{n_{GFM}} \left(P_{L_i} + \sum_{j}^{n} P_{ij} - P_{set_i} \right) - \sum_{i}^{n_{GFL}} \left(P_{L_i} + \sum_{j}^{n} P_{ij} - P_{set_i} \right) - \sum_{i}^{n_{GFL}} \left(\frac{1}{\omega_{pll_i}^2} s^2 + \frac{2\zeta_i}{\omega_{pll_i}} s \right) \Delta P_i$$

$$= - \sum_{i}^{n} P_{L_i} - \sum_{i}^{n} \sum_{j}^{n} P_{ij} + \sum_{i}^{n} P_{set_i} - \sum_{i}^{n_{GFL}} \left(\frac{1}{\omega_{pll_i}^2} s^2 + \frac{2\zeta_i}{\omega_{pll_i}} s \right) \Delta P_i$$

$$= - \left(P_{L_T} - P_{set_T} \right) - \sum_{i}^{n_{GFL}} \left(\frac{1}{\omega_{pll_i}^2} s^2 + \frac{2\zeta_i}{\omega_{pll_i}} s \right) \Delta P_i \quad (13)$$

where $P_{set_T} = \sum_i^n P_{set_i}$ is the total of power setpoints, $P_{L_T} = \sum_i^n P_{L_i}$ is the total load power, and assuming no power losses, the sum of all power flows, $\sum_i^n \sum_j^n P_{ij}$, is null.

Equating the left- and right-hand sides, (12) and (13), the swing equation for COI is obtained as (14).

$$\left(2H_T s + D_T \right) \Delta\omega_{COI} + \sum_{i}^{n} D_i \omega_{osc_i} = -\left(P_{L_T} - P_{set_T} \right) - \sum_{i}^{n_{GFL}} \left(\frac{1}{\omega_{pll_i}^2} s^2 + \frac{2\zeta_i}{\omega_{pll_i}} s \right) \Delta P_i \quad (14)$$

The COI swing equation comprises the usual inertia, damping and power terms, here formed as sums of individual GFM and GFL inertia, damping and power terms. The third term on the left-hand side represents the sum of damped oscillations of each bus frequency around the COI, and it is null with uniform damping, $D_i/H_i = \lambda$ [18]. The term on the right-hand side with the first and second derivatives of GFL power outputs originates from the GFL swing equation (9). Note that these derivatives are mathematical notations and do not reflect actual derivative operations within the GFL controllers. As shown in Fig. 3, P is an output for GFL, hence these mathematical derivatives are really an inverse view of integrals on the input δ, as is presented in (9).

C. COI transfer function

The analysis above is used to find a transfer function of the power change to the COI frequency which facilitates inclusion of the power-frequency transient behaviour of SG from (1). In this section only, the frequency oscillations around the COI are assumed negligible, hence $\omega_i = \omega_{COI}$ [32].

Consider the sum of (1) over all n_{SG} SG and of (4) over all n_{GFM} GFM in (15, 16).

$$\sum_{i}^{n_{GFM}} \left(2H_i^{GFM} s + D_i^{GFM} \right) \Delta\omega_i + \sum_{i}^{n_{SG}} \left(2H_i^{SG} s + D_i^{SG} + K_i G_i(s) \right) \Delta\omega_i = - \sum_{i}^{n_{GFM}} \Delta P_i - \sum_{i}^{n_{SG}} \Delta P_i \quad (15)$$

$$\left(2H_T^{GFM+SG} s + D_T^{GFM+SG} + \sum_{i}^{n_{SG}} K_i G_i(s) \right) \Delta\omega_{COI} = -\Delta P_T^{GFM+SG} \quad (16)$$

where $H_T^{GFM+SG} = \sum_i^{n_{GFM}} H_i^{GFM} + \sum_i^{n_{SG}} H_i^{SG}$ is the total GFM plus SG inertia, $D_T^{GFM+SG} = \sum_i^{n_{GFM}} D_i^{GFM} + \sum_i^{n_{SG}} D_i^{SG}$ is the total GFM damping plus SG and frequency-dependent load damping, and $\Delta P_T^{GFM+SG} = P_T^{GFM+SG} - P_{set_T}^{GFM+SG}$, with P_T^{GFM+SG} the total power generated by GFM plus SG and $P_{set_T}^{GFM+SG}$ the total GFM plus SG power setpoint.

For a system served by SG, GFM and GFL, the GFM and SG supply the difference between the total power consumed (which is the load power in a lossless system) and the power injected by GFL, $P_T^{GFM+SG} = P_{L_T} - P_T^{GFL}$. From this, (16) is written as (17).

$$\left(2H_T^{GFM+SG} s + D_T^{GFM+SG} + \sum_{i}^{n_{SG}} K_i G_i(s) \right) \Delta\omega_{COI} = - \left(\Delta P_{L_T} - \Delta P_T^{GFL} \right) \quad (17)$$

Next, (9) is used to give an expression for the total GFL power difference ΔP_T^{GFL} (18). It is assumed in this section that ω_{osc_i} is negligible, so $\Delta\omega_i = \Delta\omega_{COI}$.

$$\Delta P_T^{GFL} = \sum_{i}^{n_{GFL}} \Delta P_i = \sum_{i}^{n_{GFL}} - \frac{2H_i^{GFL} s + D_i^{GFL}}{\frac{1}{\omega_{pll_i}^2} s^2 + \frac{2\zeta_i}{\omega_{pll_i}} s + 1} \Delta\omega_{COI} \quad (18)$$

With some rearranging, (18) into (17) yields a transfer function for $\Delta\omega_{COI}$:

$$\Delta\omega_{COI} = \frac{-1}{N(s)} \Delta P_{L_T} \quad (19)$$

with

$$N(s) = 2H_T^{GFM+SG} s + D_T^{GFM+SG} + \sum_{i}^{n_{SG}} K_i G_i(s) + \sum_{i}^{n_{GFL}} \left(2H_i^{GFL} s + D_i^{GFL} \right) \left(\frac{1}{\omega_{pll_i}^2} s^2 + \frac{2\zeta_i}{\omega_{pll_i}} s + 1 \right)^{-1} \quad (20)$$

The inertia terms for GFM and SG have the same form and are combined as a sum. The GFM damping, which arises from the droop function, D^{GFM}, is summed with SG damping that

arises from SGs and frequency-dependent loads, D^{SG}. The SG governor droop term, K, is added in steady-state to other droop and damping coefficients to evaluate frequency deviation, but the re-heater of an SG turbine significantly influences the transient response through $G_i(s)$. Each GFL in the network adds dynamics of a second order filter to the transfer function, and the GFL contributions cannot be aggregated if the PLL parameters are dissimilar.

(19) relies on the assumption that each bus frequency does not deviate much from the COI. Although it may be an invalid assumption for some IBR networks, (19) nonetheless provides insights and confirms that GFM can provide the same type of inertia as SG. Any generation with a droop function can provide damping with GFM being the quickest, and SG and GFL delayed by $G(s)$ and PLL, respectively. PLL dynamics of a GFL are usually much faster than the re-heater of a steam-turbine SG.

D. Pre-restoration steady-state frequency

The pre-restoration steady-state frequency designates the value at which the COI frequency would settle if no action was taken by the SO and no further change in power generation or demand happened. This value would be similar to the nadir for well damped systems, and it is found by applying the final value theorem to (19) and assuming that the change in power is a step function, $\Delta P_{L_T}(s) = \frac{\Delta P_{L_T}}{s}$, in (21).

$$\begin{aligned}\lim_{t\to\infty} \Delta\omega_{COI}(t) &= \lim_{s\to 0} s\frac{-1}{N(s)}\Delta P_{L_T}(s) \\ &= \lim_{s\to 0} \frac{-1}{N(s)}\Delta P_{L_T} \\ &= \frac{-1}{D_T}\Delta P_{L_T} \end{aligned} \tag{21}$$

where D_T is the total GFM, GFL, SG damping and SG droop, $D_T = D_T^{GFM} + D_T^{GFL} + D_T^{SG} + K_T$.

Hence, all apparatuses, including GFL, are able to contribute to the frequency deviation regulation.

E. RoCoF

The RoCoF immediately after a change in power is considered for SG, GFM, GFL and COI. The oscillations of each bus frequency around the COI are no longer assumed negligible, hence each bus may have a different frequency and RoCoF.

1) Synchronous Generator and Grid-Forming inverter: As for SG RoCoF (22) [9], a GFM RoCoF (23) is obtained by neglecting the damping in the GFM swing equation (5).

$$\text{RoCoF}_i^{SG} = s\omega_i = -\frac{1}{2H_i^{SG}}\Delta P_i \tag{22}$$

$$\text{RoCoF}_i^{GFM} = s\omega_i = -\frac{1}{2H_i^{GFM}}\Delta P_i \tag{23}$$

The RoCoF of both SG and GFM depend on the power they supply immediately after the change in load, so the additional power contributions need to be identified. It is assumed that the frequency will not have changed immediately after a load change, so the power supplied by GFL inverters will not have changed and all of the change in load power must be met by SG and GFM. A "step" power flow calculation is performed to reveal the additional power supplied by each GFM and SG. Buses with GFM and SG are considered as slack buses with their voltage magnitude and angle set to the pre-change value, since the magnitude is assumed constant and the angle does not change instantaneously. Buses without SG or GFM, are considered as PV buses, with their voltage magnitude unchanged and their additional real power set to zero except for the bus where the load change was applied. If the change in load happens at a GFM or SG bus, it is initially met entirely by the inverter or machine at that bus, and the initial RoCoF at all other GFM or SG buses is null. If the change does not happen at an SG or GFM bus, the participation of each GFM and SG is determined by the network topology and line impedances.

2) Grid-Following inverter: It is not possible to obtain an expression for GFL RoCoF from its swing equation because of the PLL second order dynamics, that appear in the swing equation. The approach is to consider first the linearisation of the power generated by GFL at bus i in (25).

$$P_i = P_{L_i} + \sum_j^n P_{ij} \tag{24}$$

$$\Delta P_i = \Delta P_{L_i} + \sum_j^n \frac{V_i V_j}{X_{ij}}(\Delta\delta_i - \Delta\delta_j) \tag{25}$$

Second, consider the linearisation (27) of the PLL equation (6) rearranged as (26).

$$\omega_i^c = (k_{P_i} + \frac{k_{I_i}}{s})\frac{\omega_i - \omega_i^c}{s} \tag{26}$$

$$\begin{aligned}\Delta\omega_i^c &= (k_{P_i} + \frac{k_{I_i}}{s})(\Delta\delta_i - \Delta\vartheta_i^c) \\ &\approx k_{P_i}\Delta\delta_i = 2\zeta_i\omega_{pll_i}\Delta\delta_i \end{aligned} \tag{27}$$

where $k_{P_i} = 2\zeta_i\omega_{pll_i}$ and $k_{I_i} = \omega_{pll_i}^2$ are respectively the proportional and integral terms of the GFL PLL, $\vartheta_i^c = \frac{\omega_i^c}{s}$ is the PLL angle that is assumed to remain constant immediately after a load change. Similarly, in this time-frame the integral term is ignored in (27). Equation (27) into (7) gives (28). Equations (28) and (25) are equated in (29).

$$\begin{aligned}\Delta P_i &= -\frac{1}{m_{P_i}} 2\zeta_i\omega_{pll_i}\Delta\delta_i \\ &= -2\omega_{pll_i}^2 H_i^{GFL}\Delta\delta_i \end{aligned} \tag{28}$$

$$-2\omega_{pll_i}^2 H_i^{GFL}\Delta\delta_i = \Delta P_{L_i} + \sum_j^n \frac{V_i V_j}{X_{ij}}(\Delta\delta_i - \Delta\delta_j) \tag{29}$$

Rearranging and differentiating (29), the GFL RoCoF is (30).

$$RoCoF_i^{GFL} = \frac{\sum_j^n \frac{V_i V_j}{X_{ij}} RoCoF_j}{2\omega_{pll_i}^2 H_i^{GFL} + \sum_j^n \frac{V_i V_j}{X_{ij}}} \tag{30}$$

The GFL RoCoF formula obtained agrees with the fundamental property of a GFL which is to *follow* the grid frequency. Besides, note that attempting to increase the GFL inertia term does not necessarily reduce the GFL RoCoF. Considering that $2\omega_{pll_i}^2 H_i^{GFL} = \frac{2\omega_{pll_i}\zeta_i}{m_{P_i}}$, GFL inertia could be increased by reducing the droop slope, and the RoCoF would decrease. But

increasing the GFL inertia term by reducing the PLL frequency would increase the RoCoF.

One might expect, intuitively, that GFL RoCoF is determined by the RoCoF created by GFM and SG in response to the power they have to supply. A GFL with a fast PLL will quickly acknowledge the change in frequency and supply additional power, relieving SG and GFM of some of the power they must supply and reducing their RoCoF. Similarly, a GFL with lower m_{P_i} supplies a larger power for the same detected frequency change which also reduces the additional power supplied by GFM and SG, and their resulting RoCoF.

3) Centre of Inertia: The COI RoCoF is obtained by derivative upon the COI frequency (10) and using SG, GFM and GFL RoCoF (22, 23, 30) in (31).

$$RoCoF^{COI} = \frac{1}{H_T}\sum_{i}^{n} H_i RoCoF_i \tag{31}$$

Assuming that ω_{osc_i} is negligible, the COI RoCoF is simplified by applying the initial value theorem to the derivative of the COI transfer function (19) in (32).

$$\begin{aligned} RoCoF^{COI}(t=0) &= \lim_{s\to\infty} s\, RoCoF_{COI}(s) \\ &= \lim_{s\to\infty} s^2\, \omega_{COI}(s) \\ &= \lim_{s\to\infty} s\frac{-1}{N(s)}\Delta P_{L_T} \\ &= -\frac{1}{2H_T^{SG+GFM}}\Delta P_{L_T} \end{aligned} \tag{32}$$

The inertia that limits the COI RoCoF is that of SG and GFM, and they are of equal importance, whereas GFL has no contribution to limit COI RoCoF.

F. Settling time

The COI transfer function (19) is too complex to readily yield a settling time. Instead, a specific case where simplification is possible is studied. Consider a network with IBRs only and where the GFL PLLs are fast, (33) is a first order system for which the 2% settling time, t_{ss}, is (34). It depends on the total damping and the total GFM inertia. If a GFM is replaced by a GFL with same damping and a fast PLL and if the lost GFM inertia is compensated by other GFMs, then the COI response is not impacted.

$$\lim_{\omega_{pll}\to\infty} \Delta\omega_{COI} = -\frac{1}{2H_T^{GFM}s + D_T}\Delta P_{L_T} \tag{33}$$

$$t_{ss} = -\ln(0.02)\times\frac{2H_T^{GFM}}{D_T} \approx 4\times\frac{2H_T^{GFM}}{D_T} \tag{34}$$

III. Analysis Validation and Discussion

The modified IEEE 14-bus network [34] in Fig. 4 is used to validate the analysis. The SG and synchronous condensers of buses 1, 2, 3, 6 and 8 are replaced by GFM, and GFL are added at buses 11, 12 and 13 [34]. The line impedances are the same as the standard IEEE 14-bus network [35]. The configuration of the IBR controllers is as shown in Fig. 1, and the parameters of the outer loops of each IBR controller are shown in Table I, with P_{rat} the rated power. Following [36] and [37], the

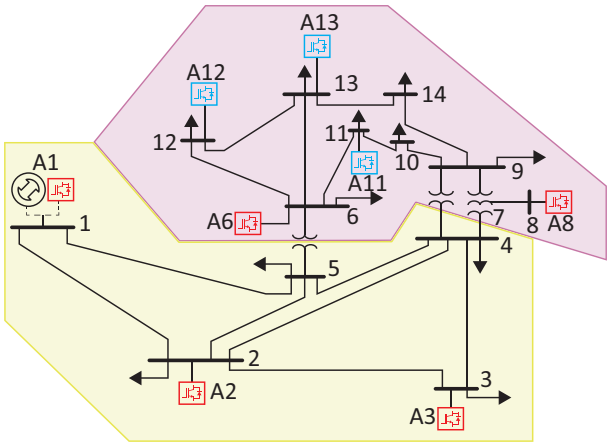


Fig. 4. Modified IEEE 14-bus network with added inverters [34], GFM are in red and GFL in blue. Either an SG or a GFM is connected to bus 1.

TABLE I
IBR OUTER LOOP PARAMETERS FOR CASE 1

Bus	Type	P_{set} (pu)	P_{rat} (pu)	Droop (%)	Bandwidth (Hz)	D_i (pu)	H_i (pu.s)
1	GFM	≈ 1	3	3	2.996	100	2.66
2	GFM	0.4	0.8	4	0.319	20	4.99
3	GFM	0.3	0.68	4.5	0.785	15	1.52
6	GFM	0.3	0.68	4.5	0.995	15	1.20
8	GFM	0.3	0.68	4.5	0.995	15	1.20
11	GFL	0.1	0.1	5	10	2	
12	GFL	0.1	0.1	5	10	2	
13	GFL	0.1	0.1	5	10	2	
COI		2.6	6.13			171	11.57

voltage- and current-controller bandwidths of the GFM are chosen to be 300 Hz and 1,500 Hz respectively. For GFL, the power controller is static (algebraic) (35), and the current-controller bandwidth is 1,500 Hz. Apparatus parameters are detailed in Table II, and inverters themselves are represented with average models rather than switching models. The yellow area in Fig. 4 comprises of buses 1 to 5 and has a high local inertia of 9.17 pu.s compared to the purple area which is composed of buses 6 to 14 and has a local inertia of 2.4 pu.s. The trajectories of bus frequencies after a change in load are calculated from the swing equations (5, 9, 14) using Matlab. The trajectory is compared with that obtained from an EMT simulation (with 40 µs time-step) in Matlab Simulink with the Simplus toolbox which uses the Specialized Power Systems library (previously known as SimPowerSystem) [38]. As explained in Section II-A, the swing equation model is simplified whereas the EMT simulation takes into account the dynamics of controller inner loops, the voltage responses at buses and the network dynamics including line resistances.

$$\begin{bmatrix} i_d^{ref} \\ i_q^{ref} \end{bmatrix} = \begin{bmatrix} V_d & V_q \\ -V_q & V_d \end{bmatrix}^{-1} \begin{bmatrix} P^{ref} \\ Q^{ref} \end{bmatrix} \tag{35}$$

The first three test cases investigate the validity of the analysis for different examples of power imbalances. In case 1, a positive step change in load of 0.1 pu at bus 10 is applied to resemble a loss of generation in the low inertia area of the network, while case 2 investigates a positive step change in load of 0.4 pu at bus 5 in the high-inertia region. In case 3,

TABLE II
APPARATUSES PARAMETERS

GFM inner loops	
Current Controller	PI, 1500 Hz
Voltage Controller	Decoupled PI, 300 Hz
GFL inner loops	
Current Controller	PI, 1500 Hz
Power Controller	Static (35)
GFM LCL filter	
Inverter-side inductor	0.159×10^{-3} pu
Inverter-side inductor inner resistance	0.01 pu
Capacitor	0.063×10^{-3} pu
Grid-side inductor	0.032×10^{-3} pu
Grid-side inductor inner resistance	0.002 pu
GFL L filter	
Inductor	0.637×10^{-3} pu
Inductor inner resistance	0.01 pu
SG parameters	
damping from SG and frequency-dependent load D^{SG}	2 pu
Servomotor time constant T_1	0.3 s
Valve bowl time constant T_2	0.05 s
Re-heater time constant T_3	10 s
Fraction of thermal energy converted to mechanical work F	0.25

a negative step change in load of 0.295 pu is applied at bus 9 to mimic a load rejection that happens when an HVDC line running on export is disconnected.

The comparison between the frequency trajectories obtained from solving the swing equations (5, 9, 14) in Matlab and that from time-step simulation of the network is shown in Fig. 5 for the GFM at bus 1 in the high inertia region, the GFL at bus 11 in the low inertia region and the COI. The frequencies are seen to be accurately modelled by their swing equations. The frequencies at the two example buses are seen to oscillate around the COI, with the frequency and amplitude of these oscillations similar in the swing equation model and the simulation and any small differences attributed to the limited bandwidth of the inverter inner loops. Similar observations apply for other buses as shown in Appendix A for case 1. Therefore, as found in [23] for a 4-bus network, the swing equations (5, 9, 14) for the frequency stability of inverters are accurate and scale up, here to a 14-bus network. In cases 1 and 3, where the change happens in the low inertia region at bus 10 and 9 respectively, the oscillations are larger in the low inertia region (bus 11) than in the high inertia region (bus 1) which is further from the change in load. In case 2, the change happens in the high inertia region, closer to bus 1 than bus 11, but the inertia of the area is significantly larger, and the oscillations at bus 1 remain small.

For a quantitative comparison, the pre-restoration steady-state frequency in Fig. 5 is 49.97 Hz, 49.88 Hz and 50.09 Hz in case 1, 2 and 3 respectively as predicted by applying (21): $\Delta\omega_{COI} = -\frac{\Delta P_{L_T}}{D_T}$. The theoretical RoCoF for GFM and COI are shown in Table III for case 1. A step power flow is used as explained in Section II, to give the theoretical ΔP_i, and the theoretical RoCoF are then calculated with (23, 30, 31). The simulated RoCoF are seen to be close to the theoretical RoCoF, but there are some significant differences, notably at bus 6. This difference is mainly due to the rough estimation of initial additional power supplied by each machine. At bus 6,

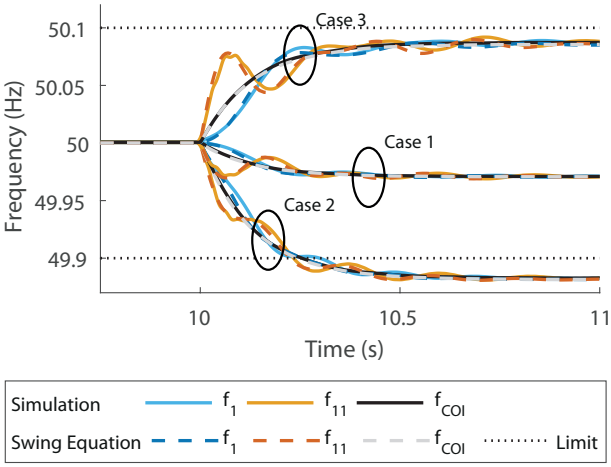


Fig. 5. Frequency trajectory of GFM bus 1, GFL bus 11 and COI for cases 1, 2 and 3 after a change in load at $t = 10$ s obtained from simulations (plain) and from swing equations (dashed)

TABLE III
ROCOF AND ADDITIONAL POWER ΔP_i SUPPLIED IN CASE 1

Local inertia	Bus i	ΔP_i (pu)		$RoCoF$ (Hz $\cdot$ s^{-1})	
		theory	simulation	theory	simulation
High	1	0.004	0.005	−0.03	−0.06
	2	0.012	0.011	−0.06	−0.06
	3	0.007	0.008	−0.12	−0.14
Low	6	0.051	0.042	−1.07	−0.86
	8	0.026	0.028	−0.53	−0.53
	11	0	0	−0.80	−0.69
	12	0	0	−0.91	−0.82
	13	0	0	−0.91	−0.79
COI		0.1	0.099	−0.21	−0.20

the initial additional power supplied observed in the simulation is 0.042 pu, which is smaller than the theoretical value of 0.051 pu. The difference is explained by the combination of two factors: first, when the step in power happens, the voltage briefly dips before returning to its initial value, and second, the analysis does not consider the transient dynamics of the line caused by the inductance (see Appendix B).

In case 1, the change in power happens in the low inertia region, and the RoCoF recorded at buses 6 and 8 (Table III) are 3 to 6 times higher than the RoCoF at buses 1 to 3 in the high inertia region. As shown in (30), the RoCoF at GFL buses largely depends on the RoCoF at other buses, hence the RoCoF at GFL buses 11, 12 and 13 are high because they follow the RoCoF at the nearby bus 6. The COI RoCoF is low at -0.2 Hz $\cdot$ s^{-1}, but all the RoCoF in the low inertia region are much higher and could trigger ± 0.5 Hz $\cdot$ s^{-1} relays.

The impact of GFL inertia on GFL RoCoF is studied through two further test cases in which the GFL inertia term is increased through adjustment of the PLL bandwidth, case 4, and droop slope, case 5. Table IV records how much the GFL RoCoF changed in these two cases from the values found in case 1 (discussed above), $RoCoF_{case\ 4\ or\ 5} - RoCoF_{case\ 1}$. The values of bandwidth and droop are shown in the table.

The GFL RoCoF observed in simulation are far from the theoretical values, but those observations should be used

TABLE IV
CHANGE IN GFL ROCOF ($\text{Hz} \cdot \text{s}^{-1}$) FOR CASES 4 AND 5 COMPARED TO CASE 1

Bus	case 4 $f_{pll} = 0.25$ Hz, $\Delta H = 1.24$s			case 5 droop $= 2.5\%$, $\Delta H = 0.03$s		
	theory	swing equation	simu-lation	theory	swing equation	simu-lation
11	-0.08	-0.03	-0.03	0.07	0.04	0.03
12	-0.12	-0.05	-0.07	0.10	0.05	0.06
13	-0.09	-0.04	-0.06	0.08	0.04	0.05

cautiously. In contrast to the frequency of a GFM, which is available directly as the reference frequency in the controller, the frequency at GFL buses must be measured from the AC signals. Here a measurement PLL, independent of the PLL used in the GFL controller, is used. The choice of bandwidth of this measurement PLL is a compromise. It is set to 100 Hz to follow the frequency with little delay but the downside of this choice is that the measurement is sensitive to noise and phase jumps. To attenuate the noise, the measured frequency is averaged over one cycle, i.e. 0.02 s. There is a significant phase jump in this experiment when the step-change in load occurs; the voltage angles of non-GFM/SG buses jump immediately after the change and continue to change rapidly thereafter. To be able to measure the initial RoCoF after the change, a good measurement of the frequency immediately after the phase jump is needed. To avoid the temporary loss of synchronisation of the measurement PLL at the phase jump, post-simulation analysis from the recorded measurement of phase voltages is preferred. The AC voltages are reversed in time so that the frequency is measured from the end of the simulation towards the step change such that the measurement PLL remains synchronised closer to the power change.

To make a fair comparison between the expected and the measured (simulation) RoCoF for GFL, a further set of results was created, labeled "swing equation" in Table IV, by applying the same measurement processing steps described above to the frequency calculated from the swing equations. These results show a smaller difference in RoCoF compared to case 1 indicating that the differences between swing equation and simulation arise mostly from the measurement processing.

The changes in RoCoF compared to case 1 are in the expected direction notwithstanding any measurement artifact. With the reduced PLL bandwidth in case 4, the GFL respond more slowly to frequency change at their bus which delays their supply of additional power to the grid. As a result, the GFM/SG which determine the RoCoF have to provide additional power for longer, and a larger negative GFL RoCoF occurs. With the reduced droop in case 5, the change in frequency as measured by the PLL results in a larger additional power supplied by the GFL, such that the GFM/SG provide less additional power and their RoCoF are reduced. This is in accordance with (30) and Section II-E2.

Fig. 6 shows the simulated absolute RoCoF magnitude for cases 1, 2 and 3. In case 1, even though the COI RoCoF is below the limit of ± 0.5 $\text{Hz} \cdot \text{s}^{-1}$, the RoCoF of the GFM at buses 6 and 8 are much larger, due to their significant participation in supplying additional power and their relatively

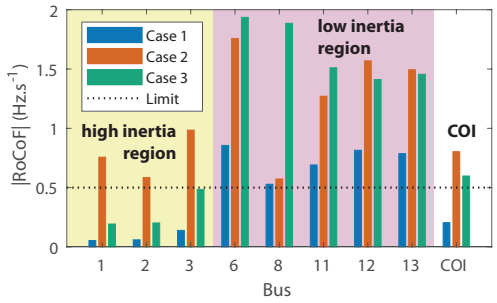


Fig. 6. Simulated absolute initial RoCoF of individual buses and COI for cases 1, 2 and 3

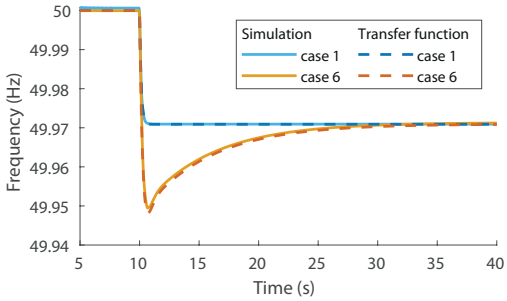


Fig. 7. COI frequency trajectory of cases 1 and 6 after a change in load at bus 10 at $t = 10$ s obtained from simulations and from transfer functions

low inertia. This leads the GFL which are in the same area as the GFM at bus 6 to also experience high RoCoF. Case 3 is similar to case 1 since the change also happens in the low inertia region, but at a higher magnitude. In case 2, the change in load happens nearest to GFM buses 1, 2, 3 and 6 which display higher RoCoF than GFM bus 8. Besides, even though the change in load is multiplied by 4 from case 1 to case 2, the RoCoF at buses 1 to 3 is multiplied by a much larger factor. This is because in case 2 the change in load happens closer to these buses which then have to contribute more to the generation of additional power. GFL which mostly follow the GFM at bus 6 also display large RoCoF. Note that the GFL RoCoF are never higher than the highest GFM RoCoF which is in accordance with (30).

Fig. 7 compares the COI frequency trajectory as calculated from the transfer function (19) to that found in the simulation. In case 6, an SG is connected to bus 1 instead of the GFM. The SG governor droop and the inertia are equivalent to the droop and inertia of the GFM being replaced: $K_1 = D_1^{GFM} = 100$ pu and $H_1^{SG} = H_1^{GFM} = 2.66$ s. The $G(s)$ parameters from (1) are in Table II. In both cases 1 and 6, the results obtained with the simulation accurately follow the prediction made with the transfer function in terms of initial RoCoF, pre-restoration steady-state frequency and overall shape. The initial COI RoCoF is the same in both cases, -0.20 $\text{Hz} \cdot \text{s}^{-1}$, and it is close to the theoretical value of -0.21 $\text{Hz} \cdot \text{s}^{-1}$, confirming that GFM contribute equivalent inertia to SG. The overall shape of case 6 is very different to case 1, the frequency of the network with IBR only is much quicker to settle as was expected by comparing the SG and GFM swing equations (1)

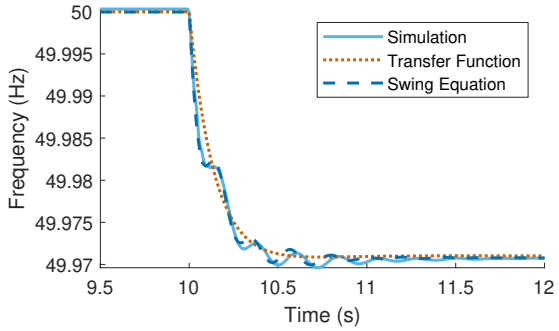


Fig. 8. COI frequency trajectory of case 4 after a change in load at bus 10 at $t = 10$ s obtained from simulations, swing equation and transfer function

and (5) where SG governor droop is delayed by $G_i(s)$.

The limitation of the COI transfer function caused by the assumption that the oscillations of each bus frequency are negligible is shown in Fig. 8 which compares the trajectory of the COI frequency in case 4 as estimated by the swing equation (14) and the transfer function (19) and as simulated. The PLL bandwidth is significantly reduced in case 4, causing large oscillations in each bus frequency which are propagated to the COI. Since the transfer function ignores these oscillations, it cannot predict them as shown in orange in Fig. 8, the trajectory obtained looks like an average of the COI frequency trajectory. Note that the swing equation is able to anticipate the oscillations in COI frequency, but it requires to also calculate each bus frequency trajectory. The simulated oscillations are slightly delayed compared to the swing equation prediction due to the processing applied to measure GFL frequencies.

Although the RoCoF study has clearly shown the need to study the frequency trajectory at each bus, the COI transfer function is still a useful quick tool to estimate the trajectory of the system frequency, and identify frequency nadirs caused by SG.

The settling time of case 6 at 21 s is much longer than that of case 1 at 0.52 s due to the SG re-heater time-constant of 10 s. Furthermore, the COI settling time of case 1, 0.52 s, is close to the minimum settling time with this combination of damping and GFM inertia, which can be calculated as 0.53 s with (34). On the other hand, for case 4, which has the same damping and GFM inertia as case 1 but with much slower GFL PLL, the settling time is 1.01 s. This is much higher than the minimum, as expected, since (34) assumes fast PLLs.

IV. Design of Frequency Trajectory

A. Proposed Design Procedure

The equations obtained for the pre-restoration frequency deviation, RoCoF and settling time are used to devise a procedure to allow SO to design the frequency trajectory through setting the droop and bandwidth parameters of GFM and GFL inverters. The requirements from National Grid ESO (NGESO) are first discussed to provide a case-study example. The largest potential loss of generation in the GB system is due to increase in 2027 from 1.4 GW set by North Sea Link to 1.8 GW set by the new Hinkley Point C power station [3]. Although a loss of this magnitude is qualified as infrequent by the SQSS standard [39], the SO must cover it. The RoCoF should be maintained below 0.5 Hz $\cdot$ s^{-1} which corresponds to an inertia of 90 GVA·s for a loss of 1.8 GW. This inertia is for the whole system which suggests that the SO's RoCoF limit applies to the COI frequency, but local RoCoF should also be considered as shown in Section III.

This procedure is designed to be applied at every trading (settlement) period when SO and resource operators (generators and energy storage) have reliable estimates of generation and demand. Resource operators should consider their forecast output power and decide how much reserve and hence damping and inertia they are willing to offer to the network. The SO, using the procedure, would determine the damping and inertia needed globally and locally to guarantee frequency stability, and choose which resources' bids to accept. IBRs then set their droop and bandwidth accordingly, and SG that are free to do so set their governor droop. The inertia contribution of SG is not flexible, but it is known as specified in the GB Grid Code [40], and it can also be estimated with novel measurement tools implemented in the grid [41].

Considering the list of credible contingencies in the network $\Delta P_{L_i}^{CC}$, the four-step procedure is:

1) Choose maximum pre-restoration frequency deviation $\Delta\omega^{max}$, and consider the maximum credible contingency
   $\rightarrow$ set total damping $D_T = \frac{\Delta P_{L_T}^{max}}{\Delta\omega^{max}}$
2) Choose maximum RoCoF $RoCoF^{max}$, and for each credible contingency
   - solve the step power flow to find how much additional power each GFM and SG would supply, ΔP_i^{CC}, and add a margin for error (to cover step power flow simplifications noted above)
   - find the local inertia needed $H_i = -\frac{|\Delta P_i^{CC}|}{2|RoCoF^{max}|}$

   $\rightarrow$ set local inertia as the maximum found over all contingencies
3) Consider settling time
   $\rightarrow$ set GFL PLL bandwidth ω_{pll_i}
4) Contract generators in the areas in need for the appropriate ancillary services of provision of inertia and damping as found in steps 1), 2) and 3).

Since inertia is set based on local needs, it is likely that the total inertia would exceed the current global requirement from NGESO. Note that small-signal stability and voltage and angle stability should still be considered alongside this procedure.

B. Procedure validation

The procedure is applied to the IBR network of Fig. 4 for cases 1, 2 and 3 where there is respectively a load change of 0.1 pu at bus 10, 0.4 pu at bus 5 or -0.295 pu at bus 9. It is arbitrarily decided that the maximum frequency deviation should be 0.1 Hz (0.002 pu), the maximum RoCoF magnitude, 0.5 Hz $\cdot$ s^{-1} (0.01 s^{-1}), and the settling time should be kept to the minimum. Limits are shown in Figs. 5 and 6. The frequency deviation exceeds the limit in case 2, and multiple local RoCoFs are higher than the RoCoF limit in all cases.

TABLE V
IBR PARAMETERS AFTER PROCEDURE

Bus i	Type	Droop (%)	Bandwidth (Hz)	D_i (pu)	H_i (pu.s)
1	GFM	3	1.879	100	4.24
2	GFM	3	0.246	26.50	8.56
3	GFM	3	0.563	22.5	3.18
6	GFM	3	0.271	22.5	6.6
8	GFM	3	0.355	22.5	5.04
11	GFL	5	10	2	
12	GFL	5	10	2	
13	GFL	5	10	2	
COI				200	25.1

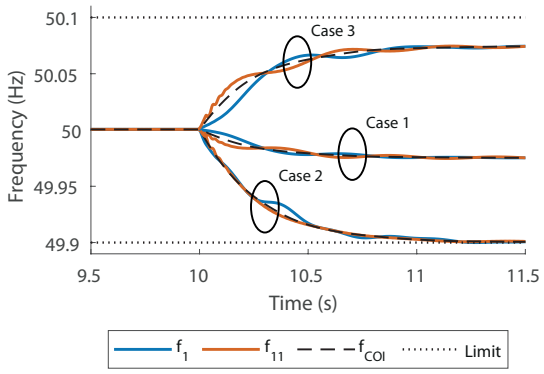


Fig. 9. Frequency trajectory of cases 1, 2 and 3 after applying the procedure obtained from simulations

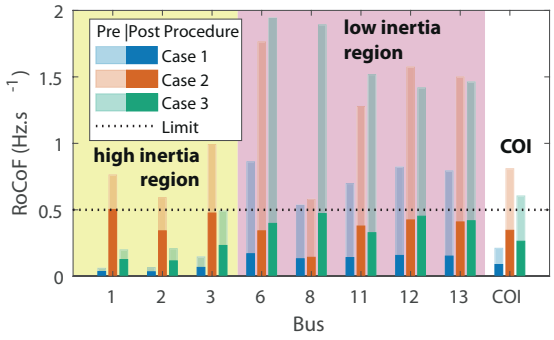


Fig. 10. Initial RoCoF magnitudes of cases 1, 2 and 3 after applying the procedure obtained from simulations

Considering first the frequency deviation, the maximum credible contigency is 0.4 pu, so the total damping must increase from 171 pu to $D_T = 0.4/0.002 = 200$ pu, using (21). The values for damping and droop at each bus are shown in Table V. Note that increased droop implies increased reserve of power. The needed inertia calculated with the second step of the procedure with a 10% margin and the corresponding bandwidths values are shown in Table V. If only the RoCoF of the COI needs to be limited, the global inertia requirement for a maximum COI RoCoF of 0.5 Hz $\cdot$ s^{-1} (0.01 s^{-1}) would be only increased to $H_T^{SG+GFM} = -\Delta P_{L_T}/(2RoCoF_{COI}^{max}) = 0.4/(2 \times 0.01) = 20$ s, using (32), whereas the total inertia is 25.1 s after the procedure.

Fig. 9 shows the resulting COI and individual bus frequencies, and the RoCoF are presented in Fig. 10. The requirements for frequency deviation and RoCoF have been respected. The frequency deviation is limited to 0.1 Hz in case 2, which was the only case that was over the limit (Fig. 5). In cases 1 and 3 where the load change happens in the previously low-inertia region, the local frequencies are now close to the COI with small oscillations due to the local inertia increased from 2.4 s to 11.64 s. The faded bars in Fig. 10 show that, before the procedure, buses 1, 2 and 3 experienced their maximum RoCoF in case 2, and buses 6 and 8, in case 3. In Fig. 10, the RoCoF at these buses is successfully reduced after the procedure. Maintaining all GFM RoCoF below 0.5 Hz $\cdot$ s^{-1} is sufficient to also maintain GFL buses below this limit. The COI RoCoF is well below the limit since the global inertia is higher than needed to only maintain the COI RoCoF below the limit. However, considering local RoCoF ensures that RoCoF relays are not triggered.

The settling time is longer at 0.98 s than case 1 (0.52 s) due to the inertia being increased by 116% but the damping by only 17%, increasing the minimum settling time to 0.98 s (34). The settling time is still close to its theoretical minimum, and the response remains much faster than obtained with a re-heat equipped SG.

V. CONCLUSION

The unification of the GFM, GFL and SG swing equations yields a COI swing equation and transfer function that accurately predict the trajectory of the system frequency after a large change in load. The analysis of the local and global frequency models produces closed-formed equations that describe the frequency deviation, RoCoF at each bus and settling time. Despite ignoring the controllers' inner loops and voltage magnitude variations, these equations give good local predictions of the key characteristics of frequency stability. The analysis provides insights into the support contributed by each type of resource. Although both GFM and GFL inverters provide damping to the network through their droop, only GFM inverters supply useful inertia equivalent to an SG. Inertia from GFL has some impact on the RoCoF, but initial RoCoF is dominated by GFM and SG. The COI analysis reveals that all the GFM inverters in a network can be aggregated and together define the minimum settling time achievable. Slow PLL of GFL increase the settling time.

A procedure was proposed, based on the local GFM and GFL swing equations, that provides a useful and quick tool to parametrise inverters in a network to meet an SO's requirement on frequency trajectory. Damping and inertia are set to achieve specified frequency deviation and RoCoF, through the droop slope and bandwidth of inverter, regardless of the proportion of GFM to GFL inverters. Furthermore, RoCoF at each bus, which can vary substantially from the COI RoCoF, can be limited by careful placement of inertia. The proposed procedure has been successfully applied to the modified IEEE 14-bus network where the desired frequency response could be achieved by properly setting the inverter parameters. The procedure relies on the assumption that voltage magnitude is constant and on a good estimation of the step power. Further

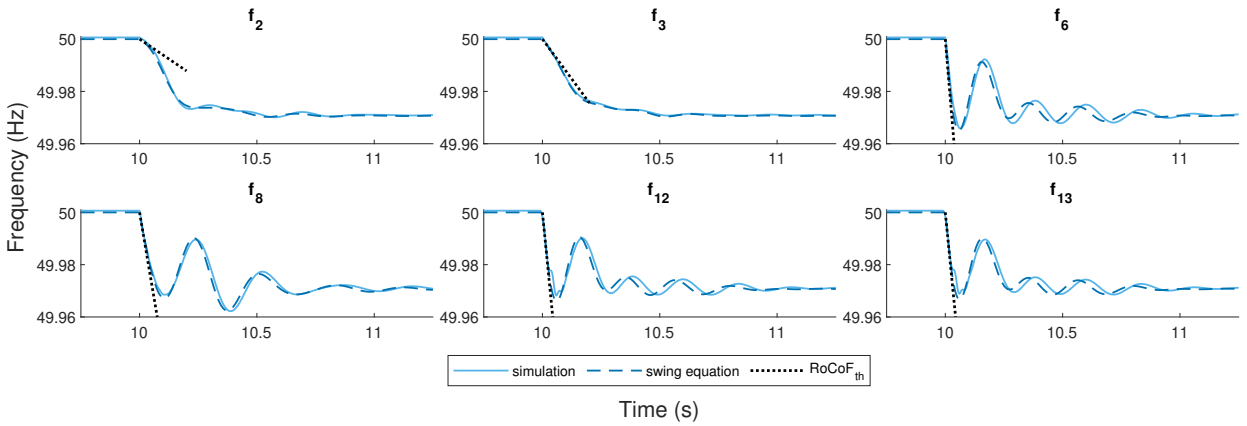


Fig. 11. Frequency trajectory of case 1 after a change in load at bus 10 at $t = 10$ s at GFM buses 2, 3, 6 and 8 and GFL buses 12 and 13 obtained from simulations (plain) and from swing equations (dashed). The initial frequency trajectory expected from the theoretical RoCoF is shown in black dotted line.

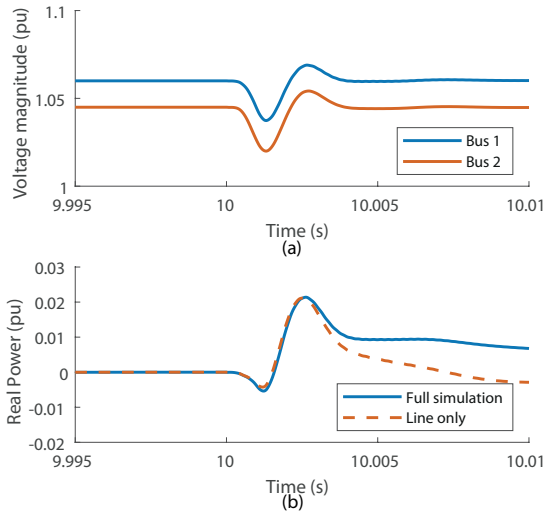


Fig. 12. (a) Voltage amplitude at buses 1 and 2 and (b) additional power flow between buses 1 and 2

works could propose alternatives to the step power flow to estimate the initial power step taking into account the change in voltage magnitude.

APPENDIX A
SWING EQUATION MODEL VS SIMULATION FOR ALL BUSES

Fig. 11 shows the comparison between the swing equation model and simulation of the frequency for the buses not shown in Fig. 5 after a change in load. Buses 1, 2, and 3 have very small oscillations compared to other buses which are closer to the bus where the load change happens. For all buses, the amplitude of oscillations are well predicted by the swing equation model. The frequency of these oscillations is also similar between the simulation and swing equation model.

APPENDIX B
IMPACT OF LINE DYNAMICS ON ROCOF

As noted in Section III, using a power flow calculation to estimate the RoCoF neglects the line reactance dynamics which are responsible for the most of the difference seen between the theoretical and measured RoCoF. To illustrate this, a change in load of $0.34\ pu$ is applied to bus 1 of the modified IEEE 14-bus network in Fig. 4, and the power flow between GFM buses 1 and 2 is considered. The assumptions made in this work imply that the GFM at bus 1 should initially provide all the additional power. The voltage magnitude and angle at GFM buses are assumed not to change initially and so the power flow between buses 1 and 2 is not expected to change and neither should the GFM at bus 2 provide any additional power. However, the simulation in Fig. 12(b) reveals that there is an immediate change in the power flow between buses 1 and 2 (plain). Fig. 12(a) shows that the voltage magnitudes at buses 1 and 2 dip immediately after the load change before rapidly recovering. This change in voltage causes a change in the rate of change of the inductor current, and hence a change in power flow in the line. To verify that the step in power flow between buses 1 and 2 is caused by the voltage magnitude dip and not a change in angle, a line identical to that between buses 1 and 2 is simulated. Voltage sources are connected at each end, and their amplitude dips as in Fig. 12(a), but with no change in angle. The resulting power flow is shown in Fig. 12(b) (dashed). The initial step in power flow of 0.02 pu matches exactly that observed in the full network simulation. After 25 ms, the line-only power flow rapidly returns to zero whereas it does not in the full simulation because the GFM voltage angles start to change. It is considered that the difference in step power predicted from the power flow and simulated in Table III is due to the assumption of constant voltage magnitude.

APPENDIX C
GFL WITH ROCOF DROOP

Some GFL droop schemes inject additional power based on the frequency deviation, but also the RoCoF (36) with n_{P_i} the RoCoF droop slope [21]. This Appendix explores the additional GFL inertia of such schemes. The RoCoF $RoCoF_i^c$ is measured through a LPF with time constant τ which filters the frequency measured by the PLL (37).

$$\Delta P_i = -\frac{1}{m_{P_i}}\Delta\omega_i^c - \frac{1}{n_{P_i}} RoCoF_i^c \tag{36}$$

$$\begin{aligned} RoCoF_i^c &= \frac{1}{\tau_i}\left(\omega_i^c - \omega_i^{cfiltered}\right) \\ &= \frac{1}{\tau_i}\left(\omega_i^c - \frac{1}{\tau_i s+1}\omega_i^c\right) \\ &= s\left(\frac{1}{\tau_i s+1}\right)\omega_i^c = s\omega_i^{cfiltered} \end{aligned} \tag{37}$$

The first part of the sum on the right-hand side of (36) is expressed as (9) with $H_i^{GFL} = \frac{\zeta_i}{m_{P_i}\omega_{pll_i}}$, and the second part as (38), using (6, 37) and $\widetilde{H}_i^{GFL} = \frac{\zeta_i}{\tau_i n_{P_i}\omega_{pll_i}}$.

$$\begin{aligned} -\frac{1}{n_{P_i}}RoCoF_i^c &= -\frac{1}{n_{P_i}}s\left(\frac{1}{\tau_i s+1}\right)\omega_i^c \\ &= -\frac{1}{n_{P_i}}s\left(\frac{1}{\tau_i s+1}\right)\frac{2\zeta_i\omega_{pll_i}s+\omega_{pll_i}^2}{s^2+2\zeta_i\omega_{pll_i}s+\omega_{pll_i}^2}\Delta\omega_i \\ &= -\frac{\frac{s}{n_{P_i}}\frac{1}{\tau_i}\left(\frac{2\zeta_i}{\omega_{pll_i}}s+1\right)}{\left(s+\frac{1}{\tau_i}\right)\left(\frac{1}{\omega_{pll_i}^2}s^2+\frac{2\zeta_i}{\omega_{pll_i}}s+1\right)}\Delta\omega_i \\ &= -\frac{\frac{2\zeta_i}{\tau_i n_{P_i}\omega_{pll_i}}s^2+\frac{1}{\tau_i n_{P_i}}s}{\left(s+\frac{1}{\tau_i}\right)\left(\frac{1}{\omega_{pll_i}^2}s^2+\frac{2\zeta_i}{\omega_{pll_i}}s+1\right)}\Delta\omega_i \\ &= -\frac{2\widetilde{H}_i^{GFL}s^2+\frac{1}{\tau_i n_{P_i}}s}{\left(s+\frac{1}{\tau_i}\right)\left(\frac{1}{\omega_{pll_i}^2}s^2+\frac{2\zeta_i}{\omega_{pll_i}}s+1\right)}\Delta\omega_i \end{aligned} \tag{38}$$

(9) and (38) into (36) gives the GFL swing equation (39).

$$\begin{aligned} \Delta P_i = &-\frac{2H_i^{GFL}s+D_i^{GFL}}{\frac{1}{\omega_{pll_i}^2}s^2+\frac{2\zeta_i}{\omega_{pll_i}}s+1}\Delta\omega_i \\ &-\frac{2\widetilde{H}_i^{GFL}s^2+\frac{1}{\tau_i n_{P_i}}s}{\left(s+\frac{1}{\tau_i}\right)\left(\frac{1}{\omega_{pll_i}^2}s^2+\frac{2\zeta_i}{\omega_{pll_i}}s+1\right)}\Delta\omega_i \end{aligned} \tag{39}$$

The same process as in Section II-E2, where slower dynamics are ignored, is applied to find the initial GFL RoCoF. (37) is approximated as (40), and (36) as (41) using (27).

$$RoCoF_i^c \approx \frac{1}{\tau_i}\Delta\omega_i^c \tag{40}$$

$$\begin{aligned} \Delta P_i &= -\frac{1}{m_{P_i}}\Delta\omega_i^c - \frac{1}{n_{P_i}}\frac{1}{\tau_i}\Delta\omega_i^c \\ &= -\left(\frac{1}{m_{P_i}}+\frac{1}{\tau_i n_{P_i}}\right)2\zeta_i\omega_{pll_i}\Delta\delta_i \\ &= -2\omega_{pll_i}^2\left(H_i^{GFL}+\widetilde{H}_i^{GFL}\right)\Delta\delta_i \end{aligned} \tag{41}$$

(41) is similar to (28) with an additional inertia term $\widetilde{H}_i^{GFL}$. Using (29, 30), the GFL RoCoF is expressed as (42).

$$RoCoF_i^{GFL} = \frac{\sum_j^n \frac{V_i V_j}{X_{ij}} RoCoF_j}{2\omega_{pll_i}^2\left(H_i^{GFL}+\widetilde{H}_i^{GFL}\right)+\sum_j^n \frac{V_i V_j}{X_{ij}}} \tag{42}$$

Adding a droop function based on a filtered RoCoF could indeed help contain the GFL RoCoF through the droop n_{P_i}. It also adds a degree of flexibility to design the frequency response through the LPF time constant τ. But the type of inertia-RoCoF relationship is the same as the controller presented in Fig. 1b, and the argument that RoCoF is mainly set by GFM remains valid.

REFERENCES

[1] HM Government, "Net Zero Strategy: Build Back Greener," Department for Business Energy and Industrial Strategy, Tech. Rep. October, 2021.

[2] J. Rocabert, A. Luna, F. Blaabjerg, and P. Rodríguez, "Control of power converters in ac microgrids," *IEEE Transactions on Power Electronics*, vol. 27, pp. 4734–4749, 2012.

[3] N. G. ESO, "Operability Strategy Report," Tech. Rep., 12 2021.

[4] J. Matevosyan, B. Badrzadeh, T. Prevost, E. Quitmann, D. Ramasubramanian, H. Urdal, S. Achilles, J. Macdowell, S. H. Huang, V. Vital, J. Osullivan, and R. Quint, "Grid-forming inverters: Are they the key for high renewable penetration?" *IEEE Power and Energy Magazine*, vol. 17, pp. 89–98, 11 2019.

[5] U. Tamrakar, D. Shrestha, M. Maharjan, B. Bhattarai, T. Hansen, and R. Tonkoski, "Virtual inertia: Current trends and future directions," *Applied Sciences*, vol. 7, p. 654, 6 2017.

[6] N. G. ESO, "National Trends and Insights - A System Operability Framework Document," Tech. Rep., 3 2021.

[7] Western Power Distribution, "Distribution System Operability Framework," Tech. Rep., 6 2018. [Online]. Available: https://www.nationalgrid.co.uk/dso/dsof

[8] S. D'Arco and J. A. Suul, "Virtual synchronous machines - Classification of implementations and analysis of equivalence to droop controllers for microgrids," in *2013 IEEE Grenoble Conference PowerTech, POWERTECH 2013*, 2013.

[9] P. Kundur, *Power system stability and control*. McGraw-Hill, 1994.

[10] D. Ramasubramanian, Z. Yu, R. Ayyanar, V. Vittal, and J. Undrill, "Converter model for representing converter interfaced generation in large scale grid simulations," *IEEE Transactions on Power Systems*, vol. 32, no. 1, pp. 765–773, 2017.

[11] B. J. Pierre, H. N. V. Pico, R. T. Elliott, J. Flicker, Y. Lin, B. B. Johnson, J. H. Eto, R. H. Lasseter, and A. Ellis, "Bulk power system dynamics with varying levels of synchronous generators and grid-forming power inverters," *Conference Record of the IEEE Photovoltaic Specialists Conference*, pp. 880–886, 6 2019.

[12] M. E. Elkhatib, W. Du, and R. H. Lasseter, "Evaluation of Inverter-based Grid Frequency Support using Frequency-Watt and Grid-Forming PV Inverters," in *2018 IEEE Power & Energy Society General Meeting (PESGM)*, 2018, pp. 1–5.

[13] W. Du, F. K. Tuffner, K. P. Schneider, R. H. Lasseter, J. Xie, Z. Chen, and B. Bhattarai, "Modeling of grid-forming and grid-following inverters for dynamic simulation of large-scale distribution systems," *IEEE Transactions on Power Delivery*, vol. 36, pp. 2035–2045, 8 2021.

[14] L. Xiong, L. Liu, X. Liu, and Y. Liu, "Frequency trajectory planning based strategy for improving frequency stability of droop-controlled inverter based standalone power systems," *IEEE Journal on Emerging and Selected Topics in Circuits and Systems*, vol. 11, pp. 176–187, 3 2021.

[15] D. Li, Q. Zhu, S. Lin, and X. Y. Bian, "A Self-Adaptive Inertia and Damping Combination Control of VSG to Support Frequency Stability," *IEEE Transactions on Energy Conversion*, vol. 32, no. 1, pp. 397–398, 2017.

[16] F. Wang, L. Zhang, X. Feng, and H. Guo, "An adaptive control strategy for virtual synchronous generator," *IEEE Transactions on Industry Applications*, vol. 54, no. 5, pp. 5124–5133, 2018.

[17] D. Doheny and M. Conlon, "Investigation into the local nature of rate of change of frequency in electrical power systems," in *2017 52nd International Universities Power Engineering Conference (UPEC)*. IEEE, 8 2017, pp. 1–6.

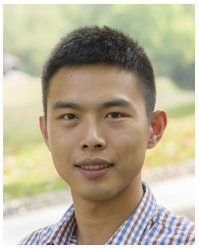
[18] K. R. Padiyar, *Structure preserving energy functions in power systems : theory and applications*. CRC Press, Taylor & Francis Group, 2013.

[19] T. S. Borsche, T. Liu, and D. J. Hill, "Effects of rotational inertia on power system damping and frequency transients," in *2015 54th IEEE Conference on Decision and Control (CDC)*, 2015, pp. 5940–5946.

[20] S. S. Guggilam, C. Zhao, E. Dall'Anese, Y. C. Chen, and S. V. Dhople, "Optimizing der participation in inertial and primary-frequency response," *IEEE Transactions on Power Systems*, vol. 33, no. 5, pp. 5194–5205, 2018.
[21] B. K. Poolla, D. Groß, and F. Dörfler, "Placement and implementation of grid-forming and grid-following virtual inertia and fast frequency response," *IEEE Transactions on Power Systems*, vol. 34, no. 4, pp. 3035–3046, 2019.
[22] Y. Jiang, A. Bernstein, P. Vorobev, and E. Mallada, "Grid-forming frequency shaping control for low-inertia power systems," *IEEE Control Systems Letters*, vol. 5, pp. 1988–1993, 12 2021.
[23] E. A. S. Ducoin, Y. Gu, B. Chaudhuri, and T. C. Green, "Swing equation modelling of GFL inverter and comparison of its damping and inertia with GFM inverter," in *19th International Conference on AC and DC Power Transmission (ACDC 2023)*, vol. 2023, 2023, pp. 108–114.
[24] J. Fang, H. Li, Y. Tang, and F. Blaabjerg, "On the inertia of future more-electronics power systems," *IEEE Journal of Emerging and Selected Topics in Power Electronics*, vol. 7, no. 4, pp. 2130–2146, 2019.
[25] S. Neira, Z. Blatsi, P. D. Judge, M. M. C. Merlin, and J. Pereda, "Modular multilevel converter with parallel branch providing integrated partially rated energy storage," *IEEE Transactions on Power Delivery*, vol. 38, no. 3, pp. 1958–1967, 2023.
[26] J. Girona-Badia, V. A. Lacerda, E. Prieto-Araujo, and O. Gomis-Bellmunt, "Limitations on the virtual inertia provision from grid-forming-connected renewable energy sources," in *19th International Conference on AC and DC Power Transmission (ACDC 2023)*, vol. 2023, 2023, pp. 166–173.
[27] P. V. Brogan, R. J. Best, D. J. Morrow, K. McKinley, and M. L. Kubik, "Effect of BESS Response on Frequency and RoCoF During Underfrequency Transients," *IEEE Transactions on Power Systems*, vol. 34, no. 1, pp. 575–583, 2019.
[28] Z. Li, Z. Cheng, J. Si, S. Zhang, L. Dong, S. Li, and Y. Gao, "Adaptive Power Point Tracking Control of PV System for Primary Frequency Regulation of AC Microgrid With High PV Integration," *IEEE Transactions on Power Systems*, vol. 36, no. 4, pp. 3129–3141, 2021.
[29] S. S. Soman, H. Zareipour, O. Malik, and P. Mandal, "A review of wind power and wind speed forecasting methods with different time horizons," in *North American Power Symposium 2010*, 2010, pp. 1–8.
[30] R. H. Inman, H. T. Pedro, and C. F. Coimbra, "Solar forecasting methods for renewable energy integration," *Progress in Energy and Combustion Science*, vol. 39, no. 6, pp. 535–576, 2013. [Online]. Available: https://www.sciencedirect.com/science/article/pii/S0360128513000294
[31] D. B. Rathnayake, M. Akrami, C. Phurailatpam, S. P. Me, S. Hadavi, G. Jayasinghe, S. Zabihi, and B. Bahrani, "Grid forming inverter modeling, control, and applications," *IEEE Access*, vol. 9, pp. 114 781–114 807, 2021.
[32] F. Milano and A. O. Manjavacas, *Dynamic State Estimation*. Wiley, 2020, pp. 227–260.
[33] P. M. Anderson and A. A. Fouad, *Power System Control and Stability*. IEEE, 2002.
[34] Y. Zhu, Y. Gu, Y. Li, and T. C. Green, "Impedance-based root-cause analysis: Comparative study of impedance models and calculation of eigenvalue sensitivity," *IEEE Transactions on Power Systems*, vol. 38, pp. 1642–1654, 3 2023.
[35] KOIOS Research and Innovation Center of Excellence, University of Cyprus. IEEE 14-bus modified test system. Accessed: 2023-08-07. [Online]. Available: https://www2.kios.ucy.ac.cy/testsystems/index.php/ieee-14-bus-modified-test-system/
[36] S. Zarei, H. Mokhtari, M. Ghasemi, S. Peyghami, P. Davari, and F. Blaabjerg, "DC-link loop bandwidth selection strategy for grid-connected inverters considering power quality requirements," *International Journal of Electrical Power & Energy Systems*, vol. 119, p. 105879, 2020.
[37] T. Green and M. Prodanović, "Control of inverter-based micro-grids," *Electric Power Systems Research*, vol. 77, no. 9, pp. 1204–1213, 2007, distributed Generation.
[38] "Simplus Grid Tool." [Online]. Available: https://github.com/Future-Power-Networks/Simplus-Grid-Tool
[39] N. G. ESO, "National Electricity Transmission System Security and Quality of Supply Standard," Tech. Rep., 2021.
[40] ——, "The Grid Code," Tech. Rep., 3 2022. [Online]. Available: https://www.nationalgrideso.com/document/162271/download
[41] NGESO. (2020) Sonar of the power grid: new inertia measurement tools planned for Great Britain's electricity system. Accessed: 2023-08-08. [Online]. Available: https://www.nationalgrideso.com/news/sonar-power-grid-new-inertia-measurement-tools-planned-great-britains-electricity-system



Eugenie A S Ducoin (S'23) received the M.Eng. degree in Electrical and Electronic Engineering with Management from Imperial College London, London, UK, in 2019. She is currently working toward the Ph.D. degree in frequency stability of power systems with high penetration levels of inverter-based resources with the Control and Power research group at Imperial College London.



Yunjie Gu (M'18-SM'20) received the B.Sc. and the Ph.D. degree in Electrical Engineering from Zhejiang University, Hangzhou, China, in 2010 and 2015 respectively. He is now a Lecturer at Imperial College London, where he was an EPSRC-funded Innovation Fellow (award EP/S000909/1). Before his academic career, he was a Consulting Engineer at General Electric Global Research Centre, Shanghai, China. His research interests include stability theory for inverter-based power systems, stability-enhancing inverter technologies, and numerical methods for computer-aided stability analysis.



Balarko Chaudhuri (M'06–SM'11) received the Ph.D. degree in Electrical and Electronic engineering from Imperial College London, London, U.K., in 2005 where he is presently a Reader in Power Systems and the Director for MSc program in Future Power Networks. His current research is on stability and control of electric power grids with high shares of variable renewable energy and inverter-based resources. He is the UK Director of the Global Centre on Electric Power Innovation for a Carbon-free Society (EPICS) and the co-lead of the workforce development pillar of the Global Power System Transformation (G-PST) consortium. He has served as an editor of IEEE Transactions on Smart Grid, IEEE Systems Journal and Elsevier Control Engineering Practice. He is a Fellow of the Institution of Engineering and Technology (IET).



Timothy C Green (F'19) received a B.Sc. (Eng) (first class honours) from Imperial College London, UK in 1986 and a Ph.D. from Heriot-Watt University, Edinburgh, UK in 1990. He is a Professor of Electrical Power Engineering and Academic Lead for Sustainability at Imperial College London. He was previously Director of the Energy Futures Lab with a role of fostering interdisciplinary research across the university. His research focuses on the role of power electronics in future power systems with very high fractions of renewable energy. In HVDC, he has contributed converter designs that strike improved trade-offs between power losses, physical size and fault handling. In distribution systems, he has pioneered the use of soft open points for relieving constraints in distribution networks. He has made important contribution to the study of stability of grids dominated by inverter-based resources. Prof. Green chairs the Engineering Advisory Council of National Grid ESO and is a member of the Advisory Council of the Electric Power Research Institute. He is a Chartered Engineering in the UK and a Fellow of the Royal Academy of Engineering and a Fellow of the Learned Society of Wales.